Cost-Effective Non-Metric Photogrammetry from Consumer-Grade sUAS: Implications for Direct Georeferencing of Structure from Motion Photogrammetry

P.E. Carbonneau[1] and J.T. Dietrich[2]

1: Department of Geography, Durham University, Lower Mountjoy site, South road, Durham, UK.

2: William H. Neukom Institute for Computational Science, Dartmouth College, Hanover, NH. USA

Abstract

The declining costs of small Unmanned Aerial systems (sUAS), in combination with Structure from Motion (SfM) photogrammetry have triggered renewed interest in image-based topography reconstruction. However, the potential uptake of sUAS-based topography is limited by the need for ground control acquired with expensive survey equipment. Direct georeferencing (DG) is a workflow that obviates ground control and uses only the camera positions to georeference the SfM results. However, the absence of ground control poses significant challenges in terms of the data quality of the final geospatial outputs. Here, we present an examination of DG carried out with consumer-grade sUAS. We begin with a study of surface deformations resulting from systematic perturbations of the radial lens distortion parameters. We then test a number of flight patterns and develop a novel error quantification method to assess the outcomes. Our perturbation analysis shows

families of predictable equifinal solutions of K_1-K_2 which minimise doming in the output model. The equifinal solutions can be expressed as $K_2 = f(K_1)$ and they have been observed for both the DJI Inspire 1 and Phantom 3 sUAS platforms. This equifinality relationship can be used as an external reliability check of the self-calibration and allow a DG workflow to produce topography exempt of non-affine deformations and with random errors of 0.1% of the flying height (*e.g.* ±5cm @ 50m), off-vertical tilts below 1° and easily-corrected linear offsets from 0.3m to 8m. Whilst not yet of survey-grade quality, these results demonstrate that low-cost sUAS are capable of producing reliable topography products without recourse to expensive survey equipment and we argue that direct georeferencing and low-cost sUAS could transform survey practices in both academic and commercial disciplines.

Keywords: sUAS, UAV, Structure from Motion, SfM, photogrammetry, Direct Georeferencing, camera calibration, Point Clouds.

Introduction

The staggering uptake of small Unmanned Aerial Systems (sUAS), commonly referred to as drones, has led some to coin the term 'the Drone Age' in reference to our era (Economist 2015). In parallel, the integration of Structure from Motion (SfM) and multi-view stereo (MVS) algorithms into the standard workflow of digital photogrammetry has led to a series of software products that can restitute topography from imagery with an unprecedented level of automation and ease (Westoby *et al.* 2012; Fonstad *et al.* 2013). Several authors have already demonstrated that imagery acquired from sUAS platforms can deliver high quality topographic survey data (Niethammer *et al.* 2012; Hugenholtz *et al.* 2013; Bemis *et al.* 2014; Immerzeel *et al.* 2014; Clapuyt *et al.* 2015; Eltner *et al.* 2015; Ryan *et al.* 2015; Turner *et al.* 2015; Woodget *et al.* 2015). The appearance of consumer-grade sUAS with imaging sensors that approach the quality of professional and scientific digital cameras is therefore precipitating a fundamental shift in topographic mapping whereby individuals or small organisations in need of such data no longer depend on national mapping agencies or geospatial/survey companies. Whilst some progress has been made towards lowering the cost of terrain mapping via digital photogrammetry *e.g.* (Carbonneau *et al.* 2003), the uptake has largely remained contained to academic circles with the commercial topographic sector currently dominated by laser-ranging technology. However, with low-cost drones and affordable SfM-photogrammetry software, photogrammetry is gaining and may return as the dominant method of topography production and become as common a tool as standard photography.

Currently, the combination of a consumer-grade sUAS equipped with a high-definition camera and free SfM-photogrammetry software, such as 123D Catch by

Autodesk or Microsoft Photosynth, can produce virtual 3D objects that are suitable for visualization or 3D printing. However, the production of topographic data and the associated orthoimagery for the purpose of formal mapping or any other scientific application is significantly more challenging and has much more stringent data quality requirements. The 3D data initially produced by SfM are not scaled and oriented to any real dimensions or directions (Westoby *et al.* 2012; Fonstad *et al.* 2013; Javernick *et al.* 2014). Therefore, SfM photogrammetry requires generally expensive survey equipment (e.g. RTK-GPS) to provide accurate (*i.e.* small mean error) and precise (*i.e.* small standard deviation of error) real-world map-coordinates of objects in the scene (*e.g.* ground control points or targets). These points are used to scale, rotate, and translate the initial model to map coordinates. However, errors present in the survey data propagate through the transformation and result in errors of scaling, rotation, and translation as illustrated in figure 1. In addition to these linear errors, detailed investigations have revealed that systematic doming deformations can often be present in the final topographic outputs for both standard photogrammetry (Wackrow and Chandler 2008, 2011) and SfM-Photogrammetry (Carbonneau and James 2012; James and Robson 2014; Woodget *et al.* 2015; Dietrich 2016). These deformations are caused by optical lens distortion (Figure 2). Figure 2a, illustrates how lens distortion can warp images. Under ideal circumstances, a lens would produce an image with a regular orthogonal grid pattern preserves straight lines and right angles. In practice, lens design and aberration effects warp the conformal image projection and result in non-right angles and curved lines with either barrel or pin-cushion distortion patterns. Furthermore, many compact lens systems, increasingly prevalent in small-format and mobile cameras, display complex patterns where the distortion is not a monotonic function of radial

distance from the centre of the image. When the lens distortions from multiple images are combined and allowed to propagate through the SfM-MVS process, the effect on the final topographic outputs is generally seen as either a doming or dishing effect (Figure 2b). Correcting the lens-distortion effects has been the focus of a very large body of work in both photogrammetry and computer vision (Brown 1966, 1971; Fraser 1997; Clarke and Fryer 1998; Luhmann *et al.* 2014). Use of the Brown-Conrady lens distortion model (table 1) is now standard practice in all forms of photogrammetry. Furthermore, the parametrisation of this model is now performed by so-called, automatic-, or on-the-job self-calibration algorithms which automatically parametrise the Brown-Conrady model, (*i.e* calibrating the camera/lens combination) from the image dataset intended for 3D reconstruction (Fraser 1997; Luhmann *et al.* 2014).

High-quality SfM-photogrammetry, therefore, requires both a correct scaling, rotation, and translation of a raw 3D point cloud and an accurate parametrisation of the Brown-Conrady lens distortion model. The dominant approach for this is the acquisition of centimetric quality ground control data (ground control points, GCPs) with professional survey equipment (e.g. RTK-GPS or total station). The photogrammetric software (standard or SfM) can then use ground control data for both georegistation and camera calibration. However, the requirement for GCPs to be acquired with survey-grade equipment remains the largest barrier, both in terms of time and cost, to the wider uptake of sUAS-based photogrammetry. The alternative is to develop so-called 'Direct Georeferencing (DG)', whereby the photogrammetric solution is determined with precise and accurate knowledge of the camera positions (X, Y, and Z) and orientation (pitch, roll, and yaw) at the time of image acquisition (Turner *et al.* 2014). This methodology is routinely used in the

case of full-sized airborne photography and LiDAR surveys (without the camera calibration requirement) and some authors have started reporting on its application to sUAS (Turner *et al.* 2014).

The advantages of DG are clear: by removing the need for ground control, professional survey equipment is no longer required, which could dramatically reduce the cost of topographic surveys (*e.g.* RTK-GPS equipment costs in excess of $10 000). Furthermore, with DG, ground access to the survey area would not be required, which would facilitate high-quality topographic monitoring in hazardous or inaccessible areas. We therefore argue that the development and wider uptake of cost-effective photogrammetry from sUAS platforms that are capable of producing outputs suitable for a range of mapping and technical applications is reliant on the further development of direct georeferencing. To a certain extent, this has already begun. In recent years, there has been an explosion of sUAS options made available to consumers and researchers, both fixed-wing and rotorcraft. They range from higher priced ready-to-fly (RTF) models to lower priced do-it-yourself or "scratch-built" options. There are now a wide range of options for consumer-grade camera drones priced from £500 to £2500. As discussed further in this paper, these drones have many desirable features for scientific mapping and they have enabled an emergence in consumer-grade photogrammetry, colloquially called '3D mapping'. However, much of this activity is not informed by photogrammetry and the specific challenges of data quality and camera calibration quality in the absences of GCPs have not been addressed in the consumer market and only researched by a few authors in academic circles (Turner *et al.* 2014; Eling *et al.* 2015; Milik and Gabrlik 2015). Direct georeferencing of SfM has been demonstrated from manned aircraft (Nolan *et al.* 2015). However, the reliability of the DG approach from consumer-

grade sUAS and its suitability as a fully-fledged topographic survey method is yet to be demonstrated.

In this paper, we deploy two popular consumer-grade sUAS models and we examine their ability to produce topography within a direct georeferencing workflow. Our approach is informed by core photogrammetry concepts and particular attention was paid to camera calibration issues: Perturbation analysis of lens distortion and corresponding doming deformations were conducted within a space of the K_1 and K_2 lens distortion parameters (Table 1). Furthermore, we develop a new approach to error assessment which is tailored to the SfM-photogrammetry workflow and explicitly determines errors in translation, rotation, scale, and surface noise and demonstrates that whilst some form of limited ground truthing is still required, survey-grade ground control is not required to achieve a satisfactory data quality.

Methods

sUAS Platforms

We deployed a Phantom 3 Professional (P3P) and an Inspire 1 (I1) both manufactured by DJI Inc. These popular quadcopters have many features of interest for scientific applications. The P3P and the I1 both have an integrated camera (Model FC300 on the P3P and Model FC350 on the I1) mounted on a three-axis gimbal that stabilizes the camera, absorbs vibrations, and compensates for the rotational motion of the quadcopter. The integrated cameras both use a wide-angle rectilinear lens and thus avoid the heavy distortions common with the fish-eye lenses employed in several drone and camera models (e.g. GoPro cameras or the DJI

Phantom 2-series). Both the P3P and I1 cameras can acquire 12-megapixel still imagery in raw (DNG) or JPEG formats. For navigation and flight stabilisation, the internal consumer-grade GPS system uses both the GNSS and GLONASS systems, increasing the number of satellites used in the GPS position determination. DJI's specifications report a GPS accuracy of ≈2.5 meters in X-Y. These positions are automatically exported to the EXIF metadata for each image in WGS84 latitude and longitude thus providing a location stamp (geotag) for each image. Finally, the low-cost of the P3P (£1200) and the I1 (£2400) make them accessible and limits the impact of a total loss in the event of a crash, allowing for flights in risky environments such as volcanos or large flood-stricken areas.

C*amera calibration experiment*

The optical components of any real lens system do not transmit light rays from the object scene to the imaging sensor in a perfectly linear manner (Wolf *et al.* 2014) . In order for SfM, or any photogrammetric method, to recover accurate 3D data defining and correcting lens distortions are a critical (Zhengyou 1996; Heikkila and Silven 1997). Lens distortions are typically generalized with two components: symmetric radial distortions and decentring (tangential) distortions (Förstner *et al.* 2013). The Brown-Conrady lens model was developed in order to correct these lens distortions. In table 1, we can see the form of the model which is based on Taylor expansions of radial, K_n and tangential P_n, distortion terms. The radial distortion parameters (K_1, K_2, and K_3) are associated with barrel and pincushion distortion patterns (Wolf *et al.* 2014) (Figure 2) and are combined to create a 2D polynomial representation of the lens distortions. The P_n terms quantify the decentring distortions, offsets of the radial distortion from the center of the image. Fraser (2013) states that there is a temptation to use the full 10-parameter form of the model to

achieve the highest possible accuracy. However, the two most critical terms in the model are the focal length (F) and K_1, followed by K_2 and the principal point coordinates (C_x, C_y) (Förstner *et al.* 2013; Wolf *et al.* 2014). For "medium accuracy" applications, K_1 is sufficient, but for higher accuracy applications, especially those utilizing wide-angle lenses (e.g. those used in modern, compact camera systems), K_2 and possibly K_3 are required (Förstner *et al.* 2013). For K_3, P_1, and P_2 to be solved accurately the image network needs to be highly redundant with a very strong, convergent geometry (Wolf *et al.* 2014), which is often only possible in highly controlled environments. It is however recognized that the K_n parameters can be highly correlated, due to the nature of the polynomial base (Zienmann 1986; Fraser 1997). Fraser (1997) suggests that statistical tests can be conducted on the parameters to determine if additional K_n parameters result in a statistically significant difference in the radial distortion profile. However, the K_n parameters are not strongly coupled to the other parameters in the model or with the external orientation parameters and therefore an over-parameterization (additional K_n terms) will still yield a valid distortion profile (Fraser 1997). Additionally, P_1 and P_2 are highly correlated with the principle point coordinates and the errors are typically small compared to the K-terms. If P_1 and P_2 are supressed (i.e. set to zero) the errors can be absorbed by C_x, C_y (Fraser 2013, Förstner et al. 2013). Förstner et al (2013) also states that the perturbations associated with P-terms are "universally ignored in analytical photogrammetry".

When errors associated with radial image distortion are allowed to propagate through the photogrammetric process, it has been established that the final topographic model can contain non-linear deformations that take form as doming or dishing of the land surface (Figure 2b) (Wackrow and Chandler 2008; James and

Robson 2014). We therefore begin with an experiment aimed at determining the optimal radial distortion parameters for the P3P and I1 lenses. We used Photoscan Professional (ver. 1.1) for all the processing described in this work. However, this software expresses the above distortion parameters in focal length units according to:

$$K_1(focal\ units) = K_1(pixel\ units) * f^2 \quad (1)$$

$$K_2(focal\ units) = K_2(pixel\ units) * f^4 \quad (2)$$

$$K_3(focal\ units) = K_3(pixel\ units) * f^6 \quad (3)$$

Where f is the focal length in pixel units. The expression of K_n in focal length units yield easily manageable numbers which can be expressed without scientific notation, but it hinders cross-comparability of calibration results with different focal lengths. Therefore, from this point onwards, we will systematically report K_n values in pixel units as converted from equations 1-3.

To identify the correct distortion parameters for our lenses, we used a systematic perturbation approach with the objective of iteratively finding the optimal K_1 and K_2 values that minimized the distortions in a flat wall test site. The sUAS were operated hand-held without propellers. By walking in front of a flat wall on the campus of Durham University (for the P3P) and Dartmouth College (for the I1) at a distance of roughly 10 meters, a series of 24 images were acquired as a series of 12 convergent viewing pairs. For each pair, the optical axis of the camera intersects the wall at ≈±45°. Our only assumption is that the wall is flat and, in keeping with the objective of direct georeferencing, no other ground validation is used. Based on our other research and recreational photogrammetry experiments and data collections, the

range of K_1 and K_2 values was set as $K_1 \in [-3.7, -1.9] \times 10^{-8}$ pixels and $K_2 \in [1.7, 7] \times 10^{-15}$ pixels converted as per equations 1-3 with a focal length of 2320.06 pixels for the P3P and 2326.07 for the I1.

Within Photoscan, the 24 flat wall images were processed in order to establish initial camera calibration values. Using the Python scripting API (application program interface) for Photoscan we were able to produce and process a total of 6232 photogrammetric blocks with the same imagery but with fixed calibration parameters spanning the full K_1-K_2 space while keeping the calibration values for the focal length, principal point offset and K_3 as per the initial self-calibration. Tangential distortion and K_4 were not used in this experiment. The resulting point clouds were exported automatically as part of the Python processing script. In Matlab, each model was centred and normalised to the same dimensions and a 3D second-order polynomial fit in (x,y) was calculated for each point-cloud data. Given that the test wall is flat, any significant doming distortions in the point clouds are detected in the second order terms of the polynomial regression. In this case, the wall was longer in the x direction and therefore we expect significant doming to be detected in the x^2 term of the polynomial. Optimal calibration parameters will be those where these second order terms are minimised (≈ 0). The compiled results of the experiments were plotted as a matrix to display the data as a function of K_1 and K_2.

Lens distortion modelling

Our personal experience with camera calibration has shown that for a given camera, the outputs of self-calibration are never identical even in cases where imagery is acquired on the same day, under similar conditions and where external validation indicates that the final topographic model is of high quality. In order to further

examine similarity in the outputs of the camera calibration as observed in the perturbation experiments, we conducted additional simulations of lens perturbations. We used a Monte Carlo framework (i.e. randomly generated perturbations) implemented in MATLAB. This random Monte Carlo approach is less computationally intensive than a full examination of the parameter space and thus facilitates the exploration of this parameter space. To start, we take the optimal K_1, K_2 and K_3 calibration parameters as determined by self-calibration in the flat wall experiment described above and we calculate the associated displacement with the Brown-Conrady model (table 1), in pixels, over a profile of 2000 pixels (the positive horizontal axis of our photographs). Then a Monte Carlo approach is used to randomly generate 1 million combinations of K_1 and K_2, once again in the interval $K_1 \in [-3.7, -1.9] \times 10^{-8}$ pixels and $K_2 \in [1.7, 7] \times 10^{-15}$ pixels (as above). For each of the parameter combinations the pixel displacement profile is re-calculated. We then take the maximum difference, irrespective of location in the distortion profile, between the simulated K1-K2 combination and the optimal K_1-K_2-K_3 calibration. Finally, the maximal difference results from the 1 million Monte Carlo samples are interpolated to a regular grid for analysis and display.

Airborne Surveys and validation

Additional experiments were conducted with the P3P at two sites in county Durham, UK. First, a fallow field in the village of Lanchester was used as the main site (Site A). This triangular field is ringed by trees and it is characterised by a curved topography which is sloping in an eastwards direction. The field is fallow with wild grasses and flowers grown to a height of 10-40cm. Second, a sports field on the grounds of Durham University was used (Site B). This area was flat and had trimmed lawn. The northern limit of the area is set by a flood levee approximately 1

meter high. Figure 3 shows an aerial view of each site. The topography of both sites was established with an RTK-GPS survey using a Leica 1200 model RTK rover and base pair. For each site, RTK-GPS points were acquired with the objective of establishing the overall shape of the area. Instead of working on a gridded basis, care was taken to capture the outer bounds of the study sites and break-lines in the local topography. The GPS base-stations were set to relative positions but post-processed with added data from a permanent base station located at Newcastle Airport. The results of the survey were two sparse GPS point datasets that captured the shape of each study site.

Flight patterns and image acquisition

Based on the work of James and Robson (2014) and Fonstad *et al.* (2013) there is a consensus view that image acquisition geometry has an impact on the quality of the outputs with convergent views and multiple flight altitudes to be preferred. We therefore designed an intuitive set of flight patterns based on reasonable combinations of altitude, camera orientation, and flight direction that are expected to illustrate both good and bad performance of the SfM-photogrammetry process and test the potential of DG. The flights were grouped in two experiments both aiming to test the effect of flight pattern and image acquisition on final model geometry (detailed in Table 2). We experimented with a combination of NADIR and convergent imagery (James and Robson 2014) . Four flight patterns were tested: 1) nadir imagery from an altitude of 60 meters; 2) nadir imagery from an altitude of 60 and 80 meters; 3) nadir imagery combined with eight convergent-view images at an altitude of 60 meters; and 4) nadir imagery at 60 and 80 meters combined with eight convergent view images acquired at 60 meters. It was found that the P3P had sufficient battery life to acquire all the imagery for these four flight patterns in one

flight. Flights began with the camera at nadir at two altitudes and ended with the series of oblique view images. In the analysis stage, the images were grouped according to the four flight patterns for both sites thus yielding eight ‘flights’ labelled A1 – A4 and B1 – B4. Finally, at the time of our experiments, the DJI firmware for both the P3P and I1 recorded the relative elevation from the launch point to the EXIF data of each photo. Before every flight, we needed to establish a zero elevation datum for the flight by taking a single image on the ground from the launch position in order to get the GPS position corresponding to the launch point.

Pre-Processing

For all 8 flights, the raw RGB images (DNG format) were converted to 48-bit TIFF imagery (16-bit per band) with Adobe Photoshop elements. No image equalisation or other such adjustments were applied. We imported the initial TIFF images into MATLAB, removed the geotag (latitude /longitude) from the EXIF data, converted and output the coordinates into UTM (Zone 30 North, WGS84) to a text file, which could be imported into Photoscan Pro. In addition, the X-Y coordinates of the launch point were used to get the absolute elevation from a hydrologically corrected SRTM dataset available from the United States Geological Survey (USGS). This value was added to the relative elevation data recorded in the image metadata thus resulting in each image defined by a 3D position in UTM coordinates with elevations above the WGS 1984 ellipsoid.

TIFF images are then imported into Photoscan Pro in separate ‘chunks’ which act as distinct processing blocks. The converted camera station coordinates were imported providing an immediate geographic reference for each block. Based on the DJI

manual, which states that the on-board GPS is accurate to 2.5 meters in X-Y, the camera position accuracy setting, in Photoscan, was set to a conservative value of 5 meters. Each image block was reconstructed using the high quality image-alignment setting followed by a dense reconstruction at a low-density setting.

Error modelling and assessment

Error and quality assessment for 3D point clouds and topography data typically relies on root mean square error (RMSE) values when compared to some ground truth-value (ASPRS 2015; Whitehead and Hugenholtz 2015). We argue that these generic metrics do not provide a full description of the possible errors associated with SfM-photogrammetry. A single RMS statistic cannot explicitly identify systematic patterns such as tilt or non-affine warp. Mapping the spatial distribution of error at checkpoints can be useful in identifying these patterns, but often low checkpoint density does not capture the full extent of any systematic distortions. In the absence of a dense network of survey-grade GCPs, the georeferencing process used in SfM-photogrammetry relies on a rigid 7-parameter transformation, errors in the ground control or camera position can propagate as errors of position, orientation, and/or scale in the model (Figure 1). Each of these errors has impacts with respect to specific applications. Position/translation errors can affect change detection studies by creating false horizontal or vertical offsets. Orientation errors, especially off-vertical rotations, will affect gravity-dependent models (i.e. flow models) by producing incorrect slopes and flow directions. Scale errors will also influence change detection and volume calculations, again by creating false horizontal or vertical offsets. A single RMSE statistic, even if accompanied by a full

error distribution, is therefore not a powerful diagnostic tool when deciding if a topographic dataset is suitable for any given application. A more process-specific error assessment approach is therefore required. We propose the following error model:

$$P_{SfM} = M_7 P_{true} + \eta \quad (4)$$

Each of the three terms in equation 4 is a point cloud: P_{true} is a reference point-cloud giving the true (i.e. ground truth) representation of the surface. P_{SfM} is the point cloud calculated by SfM-photogrammetry. The matrix factor M_7 denotes the affine rigid-body 7-parameter transform needed to scale (one parameter), rotate (3 parameters: Rφ, Rθ, Rψ), and translate (3 parameters: Tx, Ty, Tz) P_{true} in order to match P_{SfM}. η is a non-linear, non-rigid, error term (also a point cloud) which can be seen as a quasi-random field produced by noise in the SfM process. We can therefore use the standard deviation of η as a measure of precision (scatter) of P_{SfM}. This will be reported as a single number and noted as η_p.

To assess errors in the SfM reconstructions we used dGPS survey data and the open-source point cloud processing software Cloud Compare (Girardeau-Montaut 2014). The first step in the process is establishing the parameters for M_7 for all 8 experiments. We duplicated each model (A1 – A4 and B1 – B4) in Photoscan and using the point cloud editing functions, edited each model to clear all points except those around the periphery of the sites where dGPS point density was the greatest. For site A, only those points located along the unvegetated and narrow footpath that circumscribes the field were kept. For site B, only the narrow concrete border (3 cm in width) of the paved footpath and the bottom and top of the flood defence ridge were preserved. These 'hollow' clouds were imported into Cloud Compare along

with the matching dGPS data. Then, automated cloud-to-cloud registration, an iterative closest point algorithm, was employed to calculate a transformation matrix that could transform the dGPS data (P_{true}) to match the hollow P_{SfM} clouds. The resulting transformation matrix is M_7 in equation 1. The accuracy and precision of the automated cloud-to-cloud registration (i.e. co-registration) procedure were evaluated separately for sites A and B and we use the residuals of points after the adjustment as an indication of fit quality. After automated co-registration for site A, we obtain a mean residual of 5.2cm with a standard deviation of 23.4cm. For site B, we obtain a mean residual of 0.1cm and a standard deviation of 3.1 cm. The higher errors for site A are to be expected due to the presence of tall grasses which will add error in the comparison of a bare earth DSM derived from dGPS to a DTM derived from photogrammetry.

Next we calculated η with the full point clouds. In practice, we calculate η as the differences between P_{true} and P_{SfM} after the application of M_7. The transformation matrix derived from the first step was applied to the full dGPS dataset and we constructed a Delaunay mesh of the dGPS points. Then the full SfM point cloud was imported into Cloud Compare and a cloud-to-mesh distance was calculated. The advantage of using the cloud-to-mesh function is that distances between the transformed P_{true} and P_{SfM} are calculated along the Z-axis and the sign of the difference is preserved. Positive differences are above P_{true} and points with negative differences are below P_{true}. The topography at our sites was relatively flat allowing us to use the simpler cloud-to-mesh distances along the Z-axis. In more complicated terrain with vertical surfaces and/or overhangs, other differencing algorithms, such as Multiscale Model to Model Cloud Comparison (M3C2), could be used to generate the difference map (Lague *et al.* 2013) . The differences are stored as an additional

field in the point cloud, and we calculate precision by taking the standard deviation of η. Furthermore, we extracted profiles from the difference clouds (see figure 3 for profile locations) and used in conjunction with the spatial distribution of cloud-to-mesh differences we were able to check for the presence of the doming deformation associated with errors in the camera calibration process. Our main objective here was to test if a hypothesised degradation of camera calibration parameters would result in the now famous doming deformation (Wackrow and Chandler 2008, 2011; James and Robson 2014; Woodget *et al.* 2015) . In this case, the reference surface could not be taken as the dGPS surface. The presence of tall grasses on site A hides any dome since the dGPS data represents the ground and the photogrammetric point clouds represent the top of the vegetation, which is a variable 10 cm to 40 cm above the bare earth. Therefore, the profiles were based on what was assumed as the best possible reference for the top of the vegetation: flights A4 and B4. In all cases, we corrected for translation, rotation, and scaling errors with the application of the appropriate M_7 transformation matrix (as described above) prior to differencing and profile extraction.

Results

Figure 4 examines the self-calibration results for the Phantom 3 camera. For the wall experiment, the self-calibration of the image block returned a focal length of 2320.06 pixels with K_1 of -2.53 x 10^{-8} pixels^{-2}, K_2 of 3.96 x10^{-15} pixels^{-4} and K3 of -1.15 x 10^{-22} pixels^{-6}. In figure 4, we plot lens distortion profiles over the 2000 pixel positive horizontal axis of the image for each K_n component separately. The K_1 component profile has a parabolic, concave-down shape. With an opposite sign, the

K_2 component profile has concave-up shape and, especially at the edges, a similar displacement magnitude when compared to the K_1 component. Finally, the K_3 component profile can be seen to have a small contribution. Figure 5 presents the results of the Monte Carlo lens distortion simulations for both the Phantom 3 and Inspire 1 lens calibrations. These graphs display a strong degree of equifinality. Along the central diagonal, it is clear that a large range of K_1-K_2 combinations can produce lens distortion profiles which match the optimal lens calibration to within displacements of 10 pixels. Further, we see zones which match to within 5 and even 2 pixels. Crucially, these zones follow the diagonal and indicate that only certain combinations of K1 and K2 yield equifinal solutions. Given the opposing concavity of the K_1 and K_2 components seen in figure 4, this is a sensible result. Linear regression indicates that solutions similar to within 2 pixels are predicted by:

$$P3\colon K_2 = -2.7364 * 10^{-7} \times K_1 + -3.4086 * 10^{-15} \quad (5)$$

$$I1\colon K_2 = -2.7335 * 10^{-7} \times K_1 + -3.5858 * 10^{-15} \quad (6)$$

Where the domain of validity for eq. (5) is $K_1 \in$ [-2.56, -2.35] x10^{-8} pixels and $K_2 \in$ [2.97, 3.62] x10^{-15} pixels and for eq (6) is $K_1 \in$ [-2.46, -2.25] x10^{-8} pixels and $K_2 \in$ [2.52, 3.18] x10^{-15} pixels.

Figure 6 shows the output of the perturbation experiments for the P3P and I1 in raster format. Similar to figure 5, we see a strong degree of equifinality with a large range of K_1-K_2 combinations resulting in lens distortion profiles which match the optimal lens calibration to within displacements of 10 pixels. Also, we see positive curvature (pin-cushion distortion) on the top-left and negative curvature (barrel distortion) on the bottom right. In the central diagonal, we have a ledge where a

family of solutions in the K_1-K_2 parameter space that minimise doming deformations with the following fits of $K_2 = f(K_1)$, where K_n is expressed in pixel units,

$$P3P\colon\ K_2 = -2.392 * 10^8 \times K_1^3 - 18.264 \times K_1^2 - 6.924 * 10^{-7} \times K_1 - 5.887 * 10^{-15} \quad (7)$$

$$I1\colon\ K_2 = -2.781 * 10^8 \times K_1^3 + -19.604 \times K_1^2 - 6.900 * 10^{-7} \times K_1 - 5.362 * 10^{-15} \quad (8)$$

Furthermore, since each point in figure 6 is the result of a least-squares surface fitting, we examined the fit quality of all points. For the P3P, the mean R^2 is 0.94, the 5th percentile is 0.75 and the median is 0.98. For the I1 the mean R2 is 0.99, the 5th percentile is 0.99 and the median is also 0.99. Additionally, if we consider only the subset of solutions along the line of equifinality, we find that for the P3P the mean R2 is 0.97, the 5th percentile is 0.94 and the median is 0.98. For the I1, the results are the same as above with a mean R2 of 0.99, a 5th percentile of 0.99 and the median of 0.99. The differences between the P3P results and the I1 results suggest an improved matching success for the I1 which could either be due to lighting conditions, surface texture or sensor quality. Overall these statistics indicate that the wall remained reasonably flat in the entire K_1/K_2 parameter space, especially for the subset of equifinal solutions defined by equations (7) and (8). However, based on figure 5, we might expect very slight doming in the upper left and bottom right of figures 6A and 6B. Woodget *et al.* (2015) observed a doming amplitude of 1.5cm during calibration flights at similar distances. It can therefore not be ruled out that our usage of the 2nd order polynomial coefficient as a test of flatness does not capture curvature with amplitudes below ≈ 0.1% to 0.15% of flying height. Figure 6 also displays points that correspond to calibration results (in pixel units) from the flight experiments with the P3P and, for the I1, a sample of other data acquired at a variety of field sites. We can see that most, but not all, self-calibration outputs plot

near the zero distortion line. Table 3 lists the self-calibration parameters returned for the eight P3P flights. We first evaluated the self-calibration by calculating the value of K_2 as per equation (7) and then calculating the error, $K_{2\varepsilon}$, between the self-calibrated and predicted values of K_2. According to this metric, flights A1 and A2 were the furthest from the zero distortion line and flights A3, A4 and B2 the closest. Flights B1, B3 and B4 seem to be in an intermediate range. Equations 5 and 7 suggests that doming deformations present due to a mis-calibration of K_1/K_2 can be corrected with an adjustment of K_2 or K_1. Preliminary experiments with corrections derived from equation 7 were only partial successful at removing doming. We systematically observed that using pre-calibrated, fixed, values lead to a degradation of results, even when using optimal values derived from figures 5 or 6. However, constraining the corrections to the zone in figure 5 with solutions equifinal to within displacements of 2 pixels (i.e. using equation 5) was successful. When applying equation (5), K_1 values self-calibrated as being outside the domain of validity were forced to the nearest value within the domain and the K_2 value re-calculated accordingly. Figure 7 presents both self-calibrated and adjusted deformation profiles along the α to β profile in figure 3. Deformation is calculated as a given profile differenced from the optimally calibrated profiles A4 and B4. Figure 7 shows that self-calibration for flights A1 and B1 returned a strong doming deformation while self-calibration of A2 resulted in a dishing deformation. The adjusted calibration values eliminated both doming and dishing deformations. However, this has come at the cost of increased surface error (random noise). This level of random noise, η in equation 4, along with other errors, are presented in table 4. In table 4, we note that Tz (datum shifts) are large for A1 and A2, and a re-examination of table 3 shows that variations in Tz to be a part of a complex and non-intuitive response to focal length

calibration issues. According to single image geometry, the scale of the image is directly proportional to the focal length. Therefore, if we consider the calibration results for A1 and A2, we might expect that a focal length difference of 565 out of 2539 would result in a ≈22% difference in scale. Table 4 shows that this is clearly not the case with a scaling errors of 0.2% in the case of A1. Furthermore, a re-examination of the point clouds via simultaneous display for cases A1-A2 shows that these models, with focal length calibrations ranging from 1974 to 2539 have a clear vertical offset but visible scale differences in the X-Y plane. This is illustrated in figure 8, which shows raw elevation profiles for flights A1 and A2 taken from points along the α to γ cross section in figure 3. The raw elevations in figure 8 were calculated from separate DEM outputs where the exact beginning and end-points of the profiles were manually chosen from accurately visible points in the respective orthoimagery rather than from fixed coordinates. For this purpose, we used orthoimagery with a 2.5 cm resolution and we estimate that the point selection was accurate to at least 3 pixels (7.5 cm). By using recognisable conjugate points as the bounds of the profiles, any scaling errors in the models will be visible as a difference in profile length between points α and γ. However, figure 8 shows no visible difference in profile length but a significant vertical offset of ≈12 m. The exact profile length in the X-Y plane was 132.36 m for A1 and 132.79 m for A2. If we consider our estimated measurement error, we obtain a scale discrepancy of 0.26% to 0.38%. This is slightly smaller but consistent with the results in table 4, which shows scaling ranging from 99.7% to 100.9%. However, closer examination does reveal errors in the vertical scaling of the model. Figure 9 plots the full set of deformations (i.e. residuals) vs elevation. This figure shows a strong correlation between errors and elevations with large scatter capable of enveloping the profiles shown in figure 7.

Closer examinations of the data confirmed this and showed that the vertical scale was either compressed (A2) or dilated (A1). Therefore, focal length calibration remains crucial. In this regard, a re-examination of table 3 shows that imagery acquired at nadir viewing angles (A1, A2, B1 and B2) leads to poor focal length calibrations whilst focal lengths calibrated from convergent view acquisitions (A3, A4, B3 and B4) are all consistent with the initial flat wall experiment.

Overall, the results for rotation, scale, and random error are very encouraging. In terms of rotation, $R\varphi$ is a rotation around the vertical axis (Z) and therefore leads to errors in the azimuths of the model. $R\theta$ is rotation around the X-axis (north and south tilt, after application of $R\varphi$). This therefore represents a rotation away from verticality and should be considered as an important source of error for surface process science applications. Finally, $R\psi$ gives the rotation around the Y-axis (east and west tit) after the application of $R\varphi$ and $R\theta$. Values of $R\theta$ are encouraging, most values are below 1 degree and as low as -0.12 degrees. As a reference, our maximum and minimum $R\theta$ errors of 2.42 and -1.42 degrees would translate as vertical errors of 4.23 m and -2.48 m (respectively) at a distance of 100 m from the rotation centre. Errors in the scaling parameter are also a potentially important since they will affect any measurements of distance and volume. The results are again encouraging with several values being within ±1% of the correct scale (i.e. 99-101%). However, some results are poor with the minimum value of 94.9% for B3 and a maximum value 104.8% for B4. Random error (η_p) values are also encouraging. Given the non-uniform vegetation present at site A, we would expect an precision of 0.3-0.4m when comparing the photogrammetric point clouds to the

dGPS bare earth surface. However, at site B the short-cropped lawn should have little impact on the data. This is consistent with the data in table 4 where random errors are in the area of 0.4 m for site A and as low as 0.06 m for site B. This promising result of 0.06, at a flying height of 60m, m would indicate an optimal precision of 0.1% (1:1000) of flying height.

Discussion

Our results demonstrate that Direct Georeferencing from low-cost aerial platforms is a viable workflow for high-quality topography mapping. Predictable equifinality in the K_1-K_2 parameter space of calibration solutions provides a measure of external reliability capable of assessing the quality of a camera calibration without the recourse to external ground control. In optimal cases, we find that surface errors of 0.1% of flying height can be achieved. James and Robson (2012) also found a similar performance but since these authors used a network of 45 surveyed ground control points, our observation of a similar performance in a DG context is a significant step forward. Our findings further confirm the recommendations of James and Robson (2014) stating that convergent viewing angles optimise the results of camera self-calibration. However, in addition to the knowledge that convergent viewing angles are qualitatively 'good' for camera calibration, our results provide a quantitative approach to calibration assessment. We recommend the following steps (summarised in figure 10): The camera should be calibrated before aerial acquisition, 20-30 images at convergent angles should be acquired of a flat wall on a recently constructed surface with a good level of texture. In our experiments, we acquired heavily overlapping (>80%) imagery with the optical axis of the camera intersecting the wall surface at an angle of ≈±45°. Rather than implementing the computationally onerous parameter space exploration we conducted in Photoscan (leading to figure 6), we recommend that users simply self-calibrate the convergent imagery in order to obtain an assumed optimal calibration. As a check of this assumption, the flat wall surface point cloud should be regressed in a 2nd order polynomial model. The second order terms should be negligible. Once an optimal calibration value is determined, users can replace the Photoscan

parameter exploration with the low-impact Monte Carlo approach described here (leading to figure 5) to determine equifinal solutions in the K_1-K_2 (potentially adding K_3) parameter space. Our findings indicate that solutions need to be similar to within a maximum displacement of 2 pixels. However, if we consider figures 5 and 6, it becomes apparent that the acceptable domain of equifinal solutions will scale with flying height. In the case of the flat wall experiment where the effective flying height was 10 meters (roughly 20% of the width of the wall), equifinality was observed over a wide range of solutions with displacements similar to within 10 pixels. In the case of real data, the flying height was 60 meters (50% of the site width) and in this case, we found that displacements similar to 2 pixels were required. Users operating at lower altitudes can therefore expect satisfactory results from calibrations delivering lens distortions that match optimum values to displacements somewhere between 2 and 10 pixels. Based on our experience, it is recommended that at least 10% of an image dataset be acquired at convergent angles of 20°-45° off-nadir. One possible approach might be to use the 'orbit' flight function now available on most consumer-grade drones. This function allows the drone to fly a fully automated orbit around specific point at a user-determined height and radius. By setting the camera to 20°-45° off-nadir in the direction of the centre of the orbit, a set of strongly convergent images can easily be acquired to augment nadir imagery. Once real aerial survey data are processed, the resulting self-calibration can then be checked against the range of equifinal K_n parameters. Furthermore, the focal length calibration should match to within 0.1% of the initially calibrated value. Since SfM-photogrammetry packages self-calibrate the camera during the initial camera alignment stage, the calibration can be checked on a field laptop without the need for the more computationally demanding stage of dense topography reconstruction. If calibration

results are not satisfactory, we recommend adding extra convergent-view images acquired from a higher altitude. At this point in our research, we do not recommend adjusting calibration values to match equifinal K_n solutions and/or using a fixed calibration during photogrammetric processing. Figure 7 clearly shows that whilst this improves the accuracy of the model by eliminating doming and dishing, it increases surface noise and thus lowers the precision of the final model. Furthermore, calibrations values fixed to those of the flat wall experiment also produced increased levels of noise with the associated loss of precision. This is consistent with the findings of (Fraser 1997; Förstner *et al.* 2013; Fraser 2013; Wolf *et al.* 2014) that recommend on-the-job self-calibration as best-practice for small format, non-metric, photogrammetry. However, we note that our approach requires a certain pattern of lens distortion which is based in the effect of parameter correlation as discussed by Zienmann (1986) and Fraser (1997). This concept of parameter correlation for the K_n components is relatively obscure but it explains our observations of equifinality. Given the level of development and computational expense of digital photogrammetry in the 1980s and 1990s, it is not surprising that earlier authors did not examine large parameter spaces of K_n. However, in the modern context of SfM where automated camera calibration is the norm, practitioners of SfM-photogrammetry should be aware of parameter correlation and equifinality in the calibration solutions. If we examine the Brown-Conrady lens model in table 1 and the lens distortion profiles in figure 4, it can be inferred that a necessary condition for equifinality and correlation in the K_1-K_2 parameter space is opposite signs for K_1 and K_2. This is what allows for various combinations of K_1 and K_2 to compensate each other and forms the basis for the parameter correlation effect. In order to assess transferability of these findings, we conducted a survey of

a range of cameras and examined their K_n radial distortion parameters as obtained by the self-calibration algorithm in Photoscan. Table 5 shows that in all cases, K_1 and K_2 have opposite signs. This suggests that the lens distortion profile will have inflection points that require the use of at least K_1 and K_2. Therefore, it can reasonably be expected that these lenses will display some equifinality (i.e correlation between K_1 and K_2) in their own K_1-K_2 parameter spaces.

Once it is confirmed that a self-calibrated block adjustment has been achieved within a family of zero distortion solutions, the rigid-body 7-parameter transformation that is employed to transform a point cloud from the arbitrary space of the initial block adjustment to map coordinates, can successfully produce topographic models to a precision of 0.1% of flying height. This translates to decimetric precisions at altitudes less than 100m AGL. These findings have significant implications for surface process studies where the DG workflow from low-cost drones offers the potential for easy and rapid topographic surveys, which are suited to a wide range of study environments including hazard-stricken and inaccessible areas. In the commercial sector, the use of drones and the DG workflow could provide a low-cost alternative to laser range-finding based approaches. If future research can improve the quality of DG-derived topography, the DG-workflow might out-compete laser scanning for certain applications with much smaller operational and capital costs. We therefore argue that the combination of low-cost drones, low-cost SfM-photogrammetry and a DG workflow will transform mapping by allowing both specialists and non-specialists to generate topography and 3D virtual landscapes with meaningful levels of accuracy and precision.

We will now proceed to a closer examination of the errors and likely sources that affect the direct georeferencing approach with sUAS and propose a few simple steps

that will improve both the accuracy and precision of the resulting topographic models. Generally, table 4 shows that flight patterns with convergent views at multiple altitudes have the most reliable performance with self-calibrations that plot along the line of zero distortion in figure 6. However, there is variability that needs further consideration. Since the model is georeferenced via the image geolocations, the spatial structure of the GPS error, and the size of the overall flight path envelope relative to this GPS error, can have a significant impact on the outcome. In figure 3, we can see that Site B is significantly narrower than Site A. This might explain why the scaling errors for Site B are larger, it suggests the size and shape of the flight path envelope is crucial in averaging out GPS errors. Whilst it is generally accepted that photogrammetric errors should be reported as a fraction of the flying altitude, in this case, this should be taken with the caveat that lower flights covering a smaller area will likely have larger relative errors caused by the GPS error occupying a larger percentage of the flight path envelope.

An examination of table 4 clearly shows that the optimal precision (η_p) does not coincide with optimal scale and tilt. Corrective steps must be taken to get the best results and in fact, we find that DG from consumer-grade sUAS still requires minimal ground-truthing for most science applications. However, this ground-truthing does not necessarily require survey-grade data or equipment. Datum shift and translation errors in XY (Tx, Ty, Tz in table 4) could arguably have no impact where a single-epoch DEM is acquired for purposes such as hydrologic or hydraulic modelling. These errors are the easiest to correct as they require only one point with a known 3D position. This can be retrieved from freely available global or national datasets. However, for change detection studies, correction of these linear shifts will be critical. In these cases, any given point in the survey area which has remained static can be

used to correct translation errors. Scaling errors may have an impact on studies of erosion and volumetric change. Their correction requires 2 points with a precisely known relative distance. Fortunately, a single scale object with accurately known dimensions in the study site is sufficient. Since the scale parameter used in the 7-parameter transform is isotropic, the scale object can be in any orientation and the resulting scale correction is valid for the whole model. The accuracy of this scale correction will be a function of the size of the object. For corrections to within 0.1%, a scale object separated by 1000 pixels is required which can be obtained from larger man-made features. In certain cases, even Google Earth can provide suitable scales. In the case of B4, we used Google Earth to measure the length of a pale cement border along the path and used this measurement in Photoscan as a scale bar. This improved model quality and resulted in a scaling parameter of 100.2 % (down from 104.8%). However, readers should be cautious when using Google Earth data for accurate mapping of any sort. Google Inc. acquires data from multiple sources and there is no stated, universal, quality standard. In fact, care should be taken with scale measurements from remotely sensed imagery, often times the measurement error from certain imagery sources can be larger error than the errors from the sUAS GPS. Tilt errors are significant in the context of surface processes where models of sediment and/or water fluxes will be sensitive to gradient errors. These errors can be corrected with two scale objects set at a right angle and levelled to an accurate horizontal pitch. If using projected map coordinates, it is also recommended to use a compass to align the azimuths of these two scale objects to N-S and E-W directions. Alternatively, secondary elevation datasets with sub-metric vertical precisions might be used (i.e. existing airborne or terrestrial LiDAR). Here we recommend a simple planar detrending operation based on the difference

between the DG topography and the reference topographic data. With the growing availability of high-resolution (metric and sub-metric) datasets, correcting for datum shifts, scale and tilt is now relatively straightforward in many parts of the globe.

If survey-grade RTK-GPS is available, the workflow presented here still has implications. Traditionally, it is recommended to have in excess of 20 ground control points well distributed in the XYZ space of the study site (Carbonneau *et al.* 2003). However, in combination with a DG workflow, three to four survey-grade ground control points distributed along the periphery of the study site, preferably collocated with pseudo-invariant features, could accurately correct for datum shifts, scale, and tilt. This could allow for topographic surveys in inaccessible areas provided that the edges of these sites are accessible. In particular, change detection studies with such a DG workflow will require careful experimental design. Multiple static points in the study site will be needed to correct for scale and datum shifts. Levelled features will also be required to correct for off-vertical titl errors. Furthermore, the error tolerance of each specific study should used to establish the sUAS flying height as one thousand times the maximum error.

The residual error of 0.1% of flying height (here 0.06 m with flights at an altitude of 60 m AGL) can at best be qualified as a ‘good’ performance. With the use of GCPs, significantly better sUAS photogrammetry precisions have been reported (Eltner *et al.* 2015; Woodget *et al.* 2015) and therefore the next steps should be the understanding of DG non-affine errors. However, it is difficult to assess this explicitly. Proprietary SfM-photogrammetry software packages such as Photoscan Pro protect many details in their matching processes for commercial reasons. At the moment, carefully designed empirical experiments appear to be the only way forward and further research on the relationship between surface noise amplitude

and pattern matching performance in the DG workflow will be required to achieve survey-grade outputs. Additionally, improving the positional accuracy of each image geotag should be a priority. (Bláha *et al.* 2012) have demonstrated that sub-metric positioning of sUAS can be achieved with on-board RTK-GPS positioning. Furthermore, (Chiang *et al.* 2012) and (Milik and Gabrlik 2015) have demonstrated that when RTK-GPS positioning is propagated through a photogrammetric solution, the position of GCPs can also be predicted with decimetric accuracies. Moreover, (Eling *et al.* 2015) report predictions of GCP positions with centimetric accuracy. Whilst these authors use experimental RTK-GPS equipment and high-cost platforms, low-cost RTK-GPS units are appearing. Swiftnav inc. is currently marketing their PIKSI GPS, which is a fully miniaturised GPS capable of real-time kinematic differential corrections. At a cost of ≈900 USD, the units are well suited to low-cost sUAS. Furthermore, RTK-enabled UAVs are appearing on the consumer market with models aimed at both the scientific (.*e.g* the RTK-ebee fixed-wing made by Sensefly inc.) and the cinema (*e.g.* the DJI Matrice 600 hexacopter) sectors. These units will inevitably make their way into the consumer market and we expect publications of results from these RTK-equipped platforms in the near future to strengthen the case for the use of DG in sUAS photogrammetry. However, we note that our findings re-emphasize the importance of camera calibration as a crucial factor in accurate topography reconstruction. The addition of RTK-GPS to sUAS might provide considerable improvements to the performance of the DG workflow, but it will not obviate the need for accurate camera calibration. This point emphasizes the fact that SfM-photogrammetry is in no way exempt from the principles of photogrammetry. Advances in image matching algorithms from the area of computer vision, integrated into the photrogrtammetric workflow, have clearly

enabled a step-change in image-based topography generation. However, practionners of SfM-photogrammetry still require traditional, ‘pre-SfM’ knowledge of photogrammetry. The illusion that SfM is not photogrammetry must now be dispelled.

Conclusion

The problem of producing topography from directly georeferenced sUAS imagery poses many significant challenges and opportunities. When we compare our results to those published by other authors, it is clear that the DG workflow results in the expected higher levels of error. However, our results and innovative approach to error characterization indicate that current consumer-grade drones along with low cost SfM-photogrammetry packages and a DG workflow can produce topographic data with sufficient quality for a limited number of applications. Given that the cost of RTK-GPS equipment is generally above ~£10 000 and that the low-cost drones used here are in the area of £1000-£2000, our DG approach offers a reduction of costs of 2 orders of magnitude. We therefore argue that further development and integration of DG into the UAS/SfM workflow has significant implications for topographic survey that justify further research and development. The facilitation of mass-production of topographic data and associated sub-metric resolution imagery will have a transformative impact on all Earth surface process sciences as well as the topographic survey and natural disaster management industries.

Acknowledgements

The authors would like to thank Drs. Matt Westoby and Mike James for very constructive reviews. We would also like to thank Howard Harper and Max Densmore for piloting assistance during data acquisition in the UK.

References

ASPRS. 2015. "New ASPRS Positional Accuracy Standards for Digital Geospatial Data Released." *Photogrammetric Engineering & Remote Sensing* 81 (4):277-.

Bemis, Sean P., Steven Micklethwaite, Darren Turner, Mike R. James, Sinan Akciz, Sam T. Thiele, and Hasnain Ali Bangash. 2014. "Ground-based and UAV-Based photogrammetry: A multi-scale, high-resolution mapping tool for structural geology and paleoseismology." *Journal of Structural Geology* 69, Part A:163-78. doi: http://dx.doi.org/10.1016/j.jsg.2014.10.007.

Bláha, M., H. Eisenbeiss, D. Grimm, and P. Limpach. 2012. "DIRECT GEOREFERENCING OF UAVS." *Int. Arch. Photogramm. Remote Sens. Spatial Inf. Sci.* XXXVIII-1/C22:131-6. doi: 10.5194/isprsarchives-XXXVIII-1-C22-131-2011.

Brown, D.C. 1966. "Decentering distortion of lenses." *Photogrammetric Engineering* 32 (3):444-62.

Brown, D.C. 1971. "Close-range camera calibration." *Photogrammetric Engineering* 37 (8):855-66.

Carbonneau, P.E., and T.D. James. 2012. "On the Quality of Point-Clouds Derived from Sfm-Photogrammetry Applied to UAS Imagery." In *AGU*. San Francisco.

Carbonneau, Patrice E., Stuart N. Lane, and Normand E. Bergeron. 2003. "Cost-effective non-metric close-range digital photogrammetry and its application to a study of coarse gravel river beds." *International Journal of Remote Sensing* 24 (14):2837-54. doi: 10.1080/01431160110108364.

Chiang, K. W., M. L. Tsai, and C. H. Chu. 2012. "The Development of an UAV Borne Direct Georeferenced Photogrammetric Platform for Ground Control Point Free Applications." *Sensors* 12 (7):9161-80.

Clapuyt, Francois, Veerle Vanacker, and Kristof Van Oost. 2015. "Reproducibility of UAV-based earth topography reconstructions based on Structure-from-Motion algorithms." *Geomorphology*. doi: http://dx.doi.org/10.1016/j.geomorph.2015.05.011.

Clarke, T. A., and J. G. Fryer. 1998. "The development of camera calibration methods and models." *Photogrammetric Record* 16 (91):51-66. doi: Doi 10.1111/0031-868x.00113.

Dietrich, J. T. 2016. "Riverscape mapping with helicopter-based Structure-from-Motion photogrammetry." *Geomorphology* 252:144-57. doi: 10.1016/j.geomorph.2015.05.008.

Economist. 2015. "Welcome to the drone age." In *The Economist*.

Eling, C., M. Wieland, C. Hess, L. Klingbeil, and H. Kuhlmann. 2015. "DEVELOPMENT AND EVALUATION OF A UAV BASED MAPPING SYSTEM FOR REMOTE SENSING AND SURVEYING APPLICATIONS." *Int. Arch. Photogramm. Remote Sens. Spatial Inf. Sci.* XL-1/W4:233-9. doi: 10.5194/isprsarchives-XL-1-W4-233-2015.

Eltner, Anette, Philipp Baumgart, Hans-Gerd Maas, and Dominik Faust. 2015. "Multi-temporal UAV data for automatic measurement of rill and interrill erosion on loess soil." *Earth Surface Processes and Landforms* 40 (6):741-55. doi: 10.1002/esp.3673.

Fonstad, M. A., J. T. Dietrich, B. C. Courville, J. L. Jensen, and P. E. Carbonneau. 2013. "Topographic structure from motion: a new development in photogrammetric measurement." *Earth Surface Processes and Landforms* 38 (4):421-30. doi: Doi 10.1002/Esp.3366.

Förstner, Wolfgang, Bernhard Wrobel, Fidel Paderes, Clive S. Fraser, John Dolloff, Edward M. Mikhail, and Wasin Rajikietgumjorn. 2013. "Analytical Photogrammetric Operations." In *Manual of Photogrammetry*, edited by J. Chris McGlone and George Y.G Lee. Bethesda, Md.: American Society for Photogrammetry and Remote Sensing.

Fraser, Clive S. 1997. "Digital camera self-calibration." *Isprs Journal of Photogrammetry and Remote Sensing* 52:149-59. doi: 10.1016/S0924-2716(97)00005-1.

Fraser, Clive S. 2013. "Automatic Camera Calibration in Close Range Photogrammetry." *Photogrammetric Engineering & Remote Sensing* 79:381-8. doi: 10.14358/PERS.79.4.381.

Girardeau-Montaut, D. 2014. "Cloud Compare." In.

Heikkila, J., and O. Silven. 1997. "A four-step camera calibration procedure with implicit image correction." *1997 Ieee Computer Society Conference on Computer Vision and Pattern Recognition, Proceedings*:1106-12. doi: Doi 10.1109/Cvpr.1997.609468.

Hugenholtz, C. H., K. Whitehead, O. W. Brown, T. E. Barchyn, B. J. Moorman, A. LeClair, K. Riddell, and T. Hamilton. 2013. "Geomorphological mapping with a small unmanned aircraft system

(sUAS): Feature detection and accuracy assessment of a photogrammetrically-derived digital terrain model." *Geomorphology* 194:16-24. doi: DOI 10.1016/j.geomorph.2013.03.023.

Immerzeel, W. W., P. D. A. Kraaijenbrink, J. M. Shea, A. B. Shrestha, F. Pellicciotti, M. F. P. Bierkens, and S. M. de Jong. 2014. "High-resolution monitoring of Himalayan glacier dynamics using unmanned aerial vehicles." *Remote Sensing of Environment* 150:93-103. doi: DOI 10.1016/j.rse.2014.04.025.

James, M. R., and S. Robson. 2012. "Straightforward reconstruction of 3D surfaces and topography with a camera: Accuracy and geoscience application." *Journal of Geophysical Research-Earth Surface* 117. doi: 10.1029/2011jf002289.

James, M. R., and S. Robson. 2014. "Mitigating systematic error in topographic models derived from UAV and ground-based image networks." *Earth Surface Processes and Landforms* 39 (10):1413-20. doi: Doi 10.1002/Esp.3609.

Javernick, L., J. Brasington, and B. Caruso. 2014. "Modeling the topography of shallow braided rivers using Structure-from-Motion photogrammetry." *Geomorphology* 213:166-82. doi: DOI 10.1016/j.geomorph.2014.01.006.

Lague, D., N. Brodu, and J. Leroux. 2013. "Accurate 3D comparison of complex topography with terrestrial laser scanner: Application to the Rangitikei canyon (N-Z)." *Isprs Journal of Photogrammetry and Remote Sensing* 82:10-26.

Luhmann, T., Stuart Robson, Stephen Kyle, and Jan Boehm. 2014. *Close-range photogrammetry and 3D imaging*. 2nd edition. ed, *De Gruyter textbook*.

Milik, Adam, and Petr Gabrlik. 2015. "13th IFAC and IEEE Conference on Programmable Devices and Embedded SystemsThe Use of Direct Georeferencing in Aerial Photogrammetry with Micro UAV." *IFAC-PapersOnLine* 48 (4):380-5. doi: http://dx.doi.org/10.1016/j.ifacol.2015.07.064.

Niethammer, U., M. R. James, S. Rothmund, J. Travelletti, and M. Joswig. 2012. "UAV-based remote sensing of the Super-Sauze landslide: Evaluation and results." *Engineering Geology* 128:2-11. doi: 10.1016/j.enggeo.2011.03.012.

Nolan, M., C. Larsen, and M. Sturm. 2015. "Mapping snow depth from manned aircraft on landscape scales at centimeter resolution using structure-from-motion photogrammetry." *Cryosphere* 9 (4):1445-63. doi: 10.5194/tc-9-1445-2015.

Ryan, J. C., A. L. Hubbard, J. E. Box, J. Todd, P. Christoffersen, J. R. Carr, T. O. Holt, and N. Snooke. 2015. "UAV photogrammetry and structure from motion to assess calving dynamics at Store Glacier, a large outlet draining the Greenland ice sheet." *The Cryosphere* 9 (1):1-11. doi: 10.5194/tc-9-1-2015.

Turner, D., A. Lucieer, and S. M. de Jong. 2015. "Time Series Analysis of Landslide Dynamics Using an Unmanned Aerial Vehicle (UAV)." *Remote Sensing* 7 (2):1736-57. doi: 10.3390/rs70201736.

Turner, D., A. Lucieer, and L. Wallace. 2014. "Direct Georeferencing of Ultrahigh-Resolution UAV Imagery." *Ieee Transactions on Geoscience and Remote Sensing* 52 (5):2738-45. doi: 10.1109/Tgrs.2013.2265295.

Wackrow, R., and J. H. Chandler. 2008. "A convergent image configuration for DEM extraction that minimises the systematic effects caused by an inaccurate lens model." *Photogrammetric Record* 23 (121):6-18. doi: DOI 10.1111/j.1477-9730.2008.00467.x.

Wackrow, R., and J. H. Chandler. 2011. "Minimising systematic error surfaces in digital elevation models using oblique convergent imagery." *Photogrammetric Record* 26 (133):16-31. doi: 10.1111/j.1477-9730.2011.00623.x.

Westoby, M. J., J. Brasington, N. F. Glasser, M. J. Hambrey, and J. M. Reynolds. 2012. "'Structure-from-Motion' photogrammetry: A low-cost, effective tool for geoscience applications." *Geomorphology* 179:300-14. doi: 10.1016/j.geomorph.2012.08.021.

Whitehead, Ken, and Chris H. Hugenholtz. 2015. "Applying ASPRS Accuracy Standards to Surveys from Small Unmanned Aircraft Systems (UAS)." *Photogrammetric Engineering & Remote Sensing* 81 (10):787-93. doi: 10.14358/PERS.81.10.787.

Wolf, Paul, Bon DeWitt, and Benjamin Wilkinson. 2014. *Elements of Photogrammetry with Application in GIS*. 4th ed ed. Maidenhead: McGraw-Hill Education.
Woodget, A. S., P. E. Carbonneau, F. Visser, and I. P. Maddock. 2015. "Quantifying submerged fluvial topography using hyperspatial resolution UAS imagery and structure from motion photogrammetry." *Earth Surface Processes and Landforms* 40 (1):47-64. doi: Doi 10.1002/Esp.3613.
Zhengyou, Z. 1996. On the epipolar geometry between two images with lens distortion. Paper presented at the Pattern Recognition, 1996., Proceedings of the 13th International Conference on, 25-29 Aug 1996.
Zienmann, H. 1986. Thoughts on a standard algorithm for camera calibration. Paper presented at the ISPRS Real-time photogrammetry- a new challenge conference, Ottawa, Canada.

Tables and figures

Parameters	Description
F_x, F_y	Focal length of the camera in X and Y dimensions.
C_x, C_y	Principle point of the image (x and y image coordinates)
K_1	Second-order radial distortion
K_2	Fourth-order radial distortion
K_3	Sixth-order radial distortion
P_1, P_2	X (P_1) and Y (P_2) tangential distortion

Brown-Conrady distortional model(Brown 1966; Heikkila and Silven 1997):

$$\begin{bmatrix}\hat{x}\\ \hat{y}\end{bmatrix} = (1 + K_1 r^2 + K_2 r^4 + K_3 r^6) * \begin{bmatrix}x\\ y\end{bmatrix} + \begin{bmatrix}2P_1 xy + P_2(r^2 + 2x^2)\\ P_1(r^2 + 2y^2) + 2P_2 xy\end{bmatrix}$$

$$r = \sqrt{(x - C_x)^2 + \left(y - C_y\right)^2}$$

where: x, y are the distorted pixel coordinates; $\hat{x}, \hat{y}$ are the undistorted pixel coordinates

Table 1: Camera calibration parameters in the Brown-Conrady model.

Site A	Site B	Flight Pattern
A1	**B1**	nadir imagery from an altitude of 60 meters
A2	**B2**	nadir imagery from an altitude of 60 and 80 meters
A3	**B3**	nadir imagery combined with eight convergent-view images at an altitude of 60 meters
A4	**B4**	nadir imagery at 60 and 80 meters combined with eight convergent view images acquired at 60 meters

Table 2: Description of the 11 experimental flights.

	Site A				
Flight	**F [pix]**	**K_1 x10^{-8}**	**K_2 x10^{-15}**	**K_3 x10^{-23}**	**$K_{2\varepsilon}$ x10^{-15}**
A1: Nadir 1	**2539**	**-2.48**	**3.86**	**-9.48**	**1.69**
A2: Nadir 2	**1974**	**-2.50**	**3.83**	**-9.97**	**3.89**
A3: Oblique 1	**2317**	**-2.52**	**3.84**	**-9.69**	**0.04**
A4: Oblique 2	**2320**	**-2.52**	**3.86**	**-10.6**	**0.06**
	Site B				
B1: Nadir 1	**2304**	**-2.45**	**4.11**	**-11.9**	**0.45**
B2: Nadir 2	**2229**	**-2.58**	**4.12**	**-13.0**	**0.02**
B3: Oblique 1	**2323**	**-2.59**	**4.13**	**-13.2**	**0.18**
B4: Oblique 2	**2323**	**-2.58**	**4.10**	**-12.2**	**0.16**

Table 3. Self-Calibration outputs for all flight experiments. $K_{2\varepsilon}$ gives the error in K_2 when calibrated values of K_2 are compared to those predicted by equation 5.

	Experiment 1: Site A							
Flight	**Tx [m]**	**Ty [m]**	**Tz [m]**	**Rφ [°]**	**Rθ [°]**	**Rψ [°]**	**S [%]**	**η_p [m]**
A1: Nadir 1	**4.02**	**1.32**	**-2.48**	**-0.93**	**-0.38**	**0.40**	**99.7**	**0.46**
A2: Nadir 2	**3.31**	**-1.79**	**8.88**	**-0.60**	**-1.42**	**-0.34**	**100.9**	**0.36**
A3: Oblique 1	**0.65**	**0.35**	**3.49**	**-1.34**	**-0.44**	**-0.02**	**99.5**	**0.55**
A4: Oblique 2	**3.04**	**1.63**	**0.36**	**-0.62**	**-0.78**	**-0.18**	**100.4**	**0.32**
	Co-registration residual [m]: 0.05 ± 0.23							
	Experiment 1: Site B							
B1: Nadir 1	**0.82**	**6.38**	**-5.73**	**0.86**	**-1.20**	**1.11**	**98.4**	**0.12**
B2: Nadir 2	**-0.46**	**4.20**	**5.19**	**0.09**	**0.33**	**-0.06**	**95.8**	**0.24**
B3: Oblique 1	**0.79**	**5.85**	**1.17**	**-0.08**	**-1.05**	**0.66**	**94.9**	**0.15**
B4: Oblique 2	**-3.31**	**2.43**	**-0.49**	**0.68**	**0.23**	**0.02**	**104.6**	**0.06**
	Co-registration residual [m]: 0.00 ± 0.03							

Table 4. Error parameters for all flight experiments. $T_{x,y,z}$ give translations (systematic offsets), $R_{\varphi,\theta,\psi}$ give Euler rotation angles with R_θ being giving off-vertical tilt angles. S is the scaling error with 100% meaning that the model scale is identical to the actual scale. η_p is the precision of the final SfM point clouds, calculated as the standard deviation of the quasi-random field η. For each site, we give the overall co-registration residual estimate for the cloud alignments as accuracy ± precision where the accuracy is the mean residual and precision is one standard deviation of the residuals.

Camera	Focal [pix]	K_1 [f]	K_2 [f]	K_3 [f]
Canon EOS REBEL T2i (18-135mm Zoom @ 18 mm)	4411.34	-0.169	0.144	0.026
Canon PowerShot A3300 IS	3827.51	-0.040	0.045	-0.033
Canon PowerShot A4400 IS **	3801.63	-0.082	0.070	-0.003
Canon PowerShot S110	2930.36	-0.04	0.01	-0.01
Canon PowerShot SD1000 (IXUS 70)	1822.4	-0.17	0.25	-0.07
Canon PowerShot SX170 IS **	3823.95	-0.091	0.432	-0.877
LG Nexus 5 **	3019.65	-0.215	0.385	-0.078
Microdrone 2.0 HD	1466.43	0.20	-1.40	3.00
Nikon D1X 35mm lens*	4535.33	-0.10	0.16	-0.12
Nikon D5200 (18-55mm Zoom @ 18mm) **	4635.72	-0.102	0.065	-0.079
Sony Nex-7, 20mm lens	5231.44	-0.15	0.13	0.03

* Traditional airborne survey pattern, acquired at nadir with 2 altitudes.

** Parameters derived from the camera calibration operations in OpenCV (opencv.org)

Table 5: Calibrated focal lengths and K_n parameters for a selection of cameras. Most of the calibration data was extracted from real surveys processed with Photoscan. Four of the cameras were calibrated with the camera calibration operations in the OpenCV software libraries. All of the cameras tested have opposite signed K_1 and K_2 values.

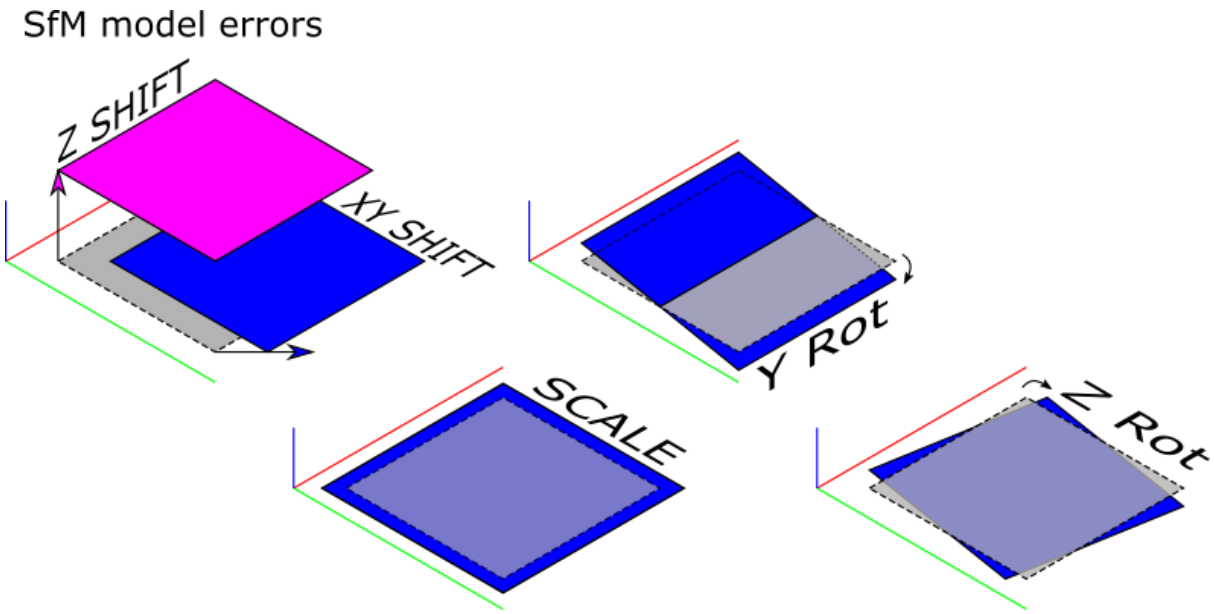

Figure 1: Potential affine model errors in SfM models. The grey squares represent the ideal orientation; the blue and magenta represent the expression of the different affine errors types. The axes in the illustration are 3D (green = x, red = y, blue = z).

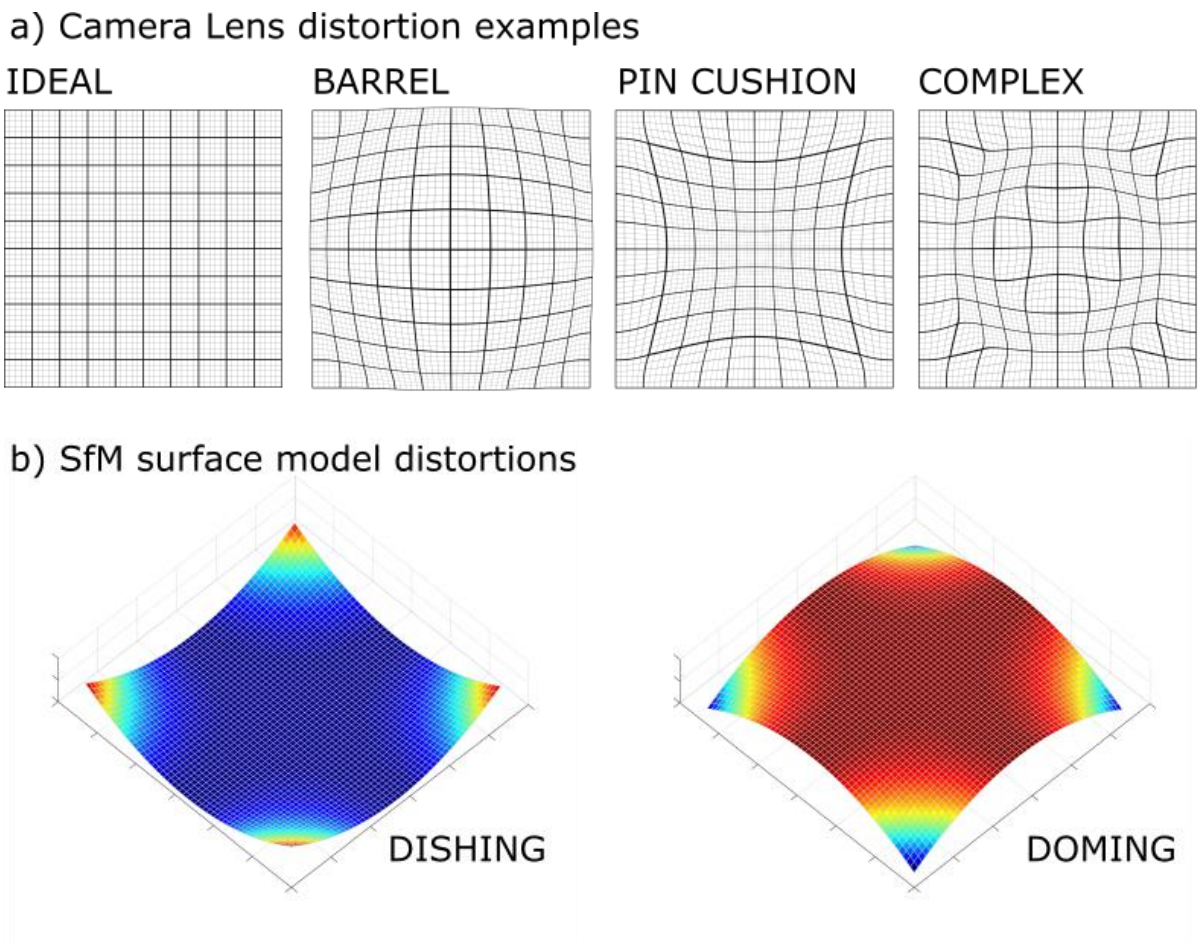

Figure 2. (a) Lens distortion examples, the ideal distortion pattern represents a lens with no distortion. The barrel and pin cushion distortions can characterised by either a positive or negative K_1 parameter. Most modern lens system in compact cameras have complex lens distortions that require more than that a single K_1 parameter, and often need a K_2 and K_3. (b) Illustration of systematic doming and dishing distortions that can present in SfM models. These errors are often attributed to incorrect survey patterns or incorrect lens distortion corrections (the colour ramp is relative, red = higher elevation, blue = lower elevations).

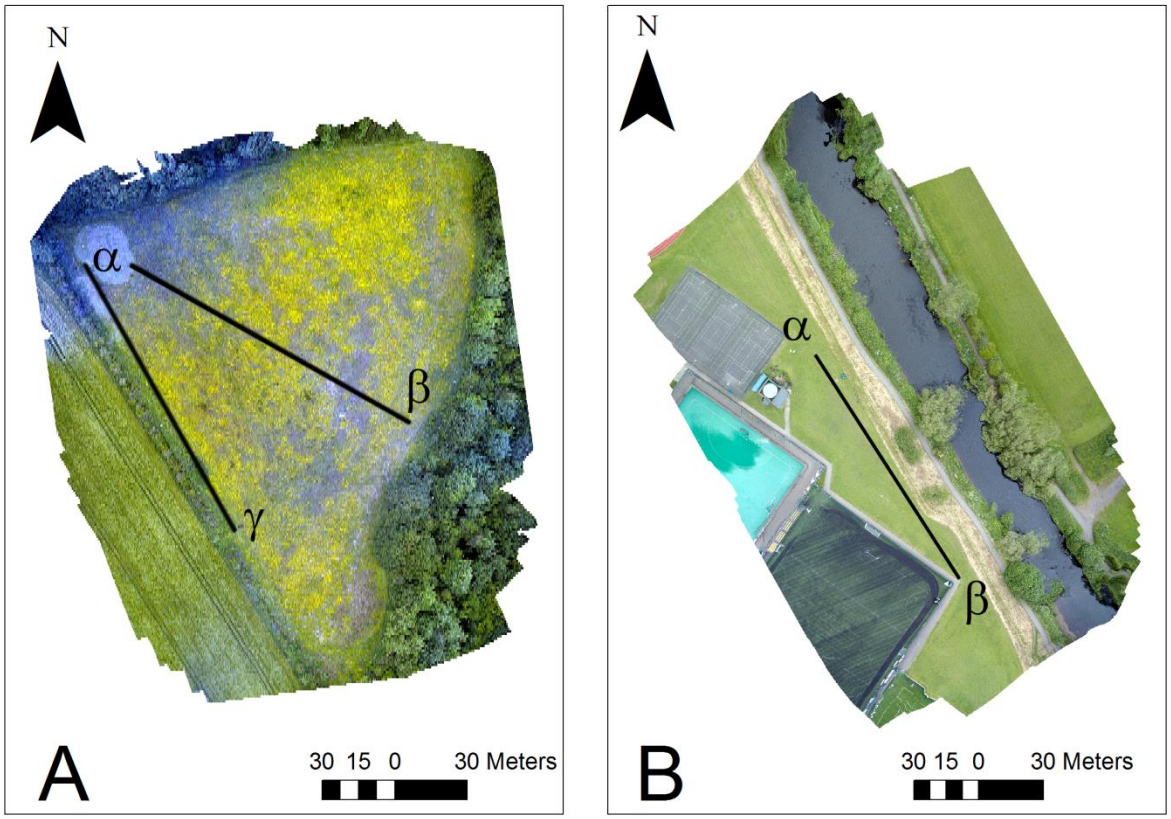

Figure 3. Study sites A and B near Durham UK, with profiles locations used in figures 7 and 8. The colour difference in the site A image (around α) was due to blending errors in orthophotograph for this shadowed area.

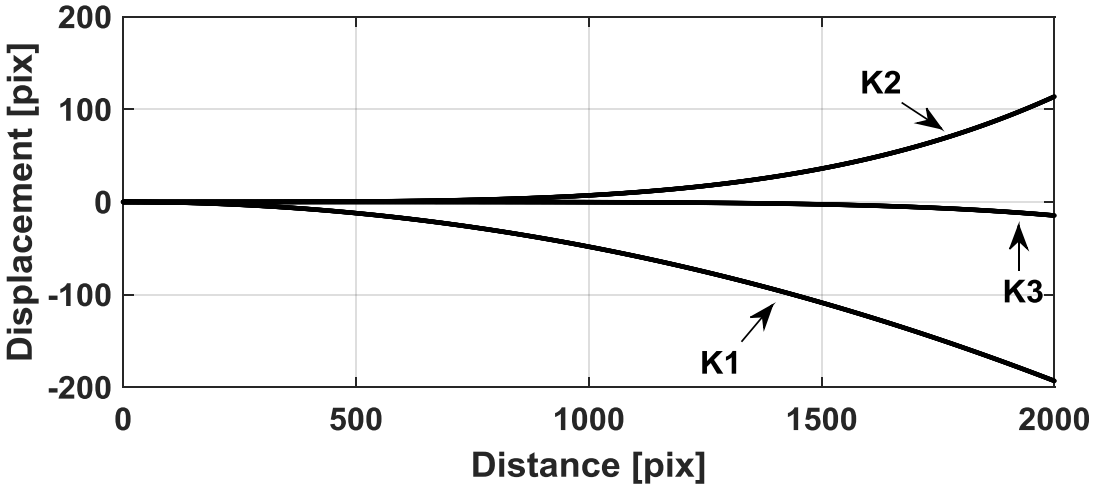

Figure 4. Lens distortion profiles for the P3P. K_1, K_2 and K_3 components of the optimal lens distortion profile for the Phantom 3 as derived from the flat wall experiment. Note the comparable magnitudes of the K_1 and K_2 contributions in the outer portion (>1500 pixels) of the profile.

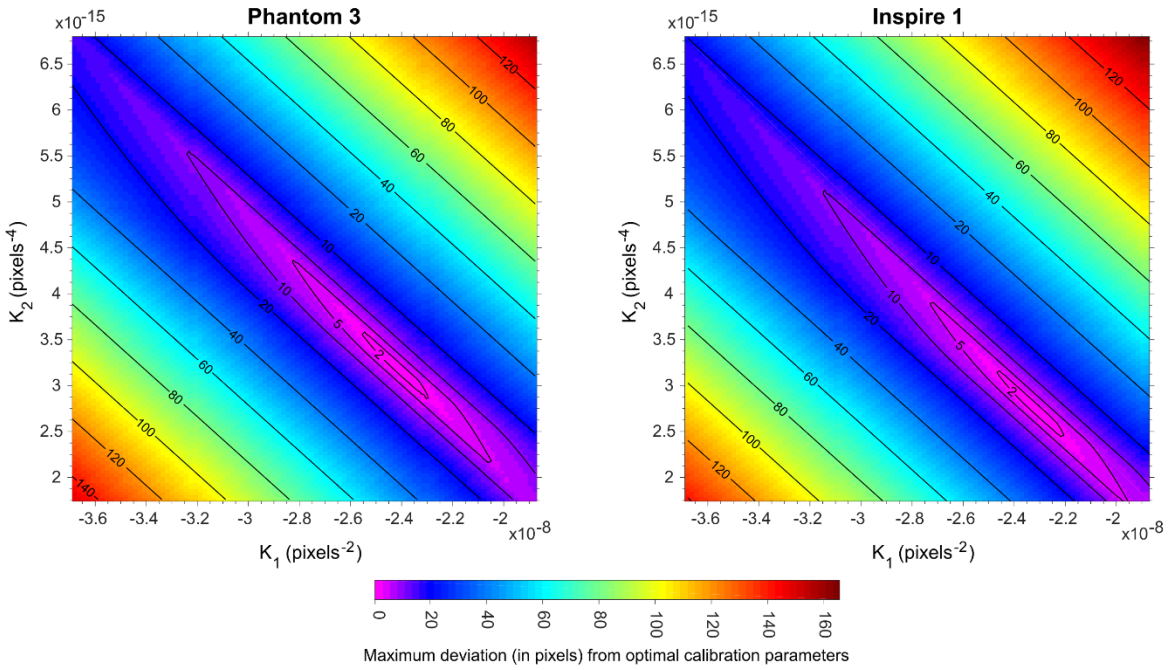

Figure 5. Equifinality in K_1-K_2 space for the Phantom 3 and Inspire 1 lenses. Colour scales and contours represent the maximum deviation, in pixels, for a given set of (K_1, K_2) values when compared to the optimal calibration parameters. We note a wide range of solutions equifinal to within 0.01 pixels.

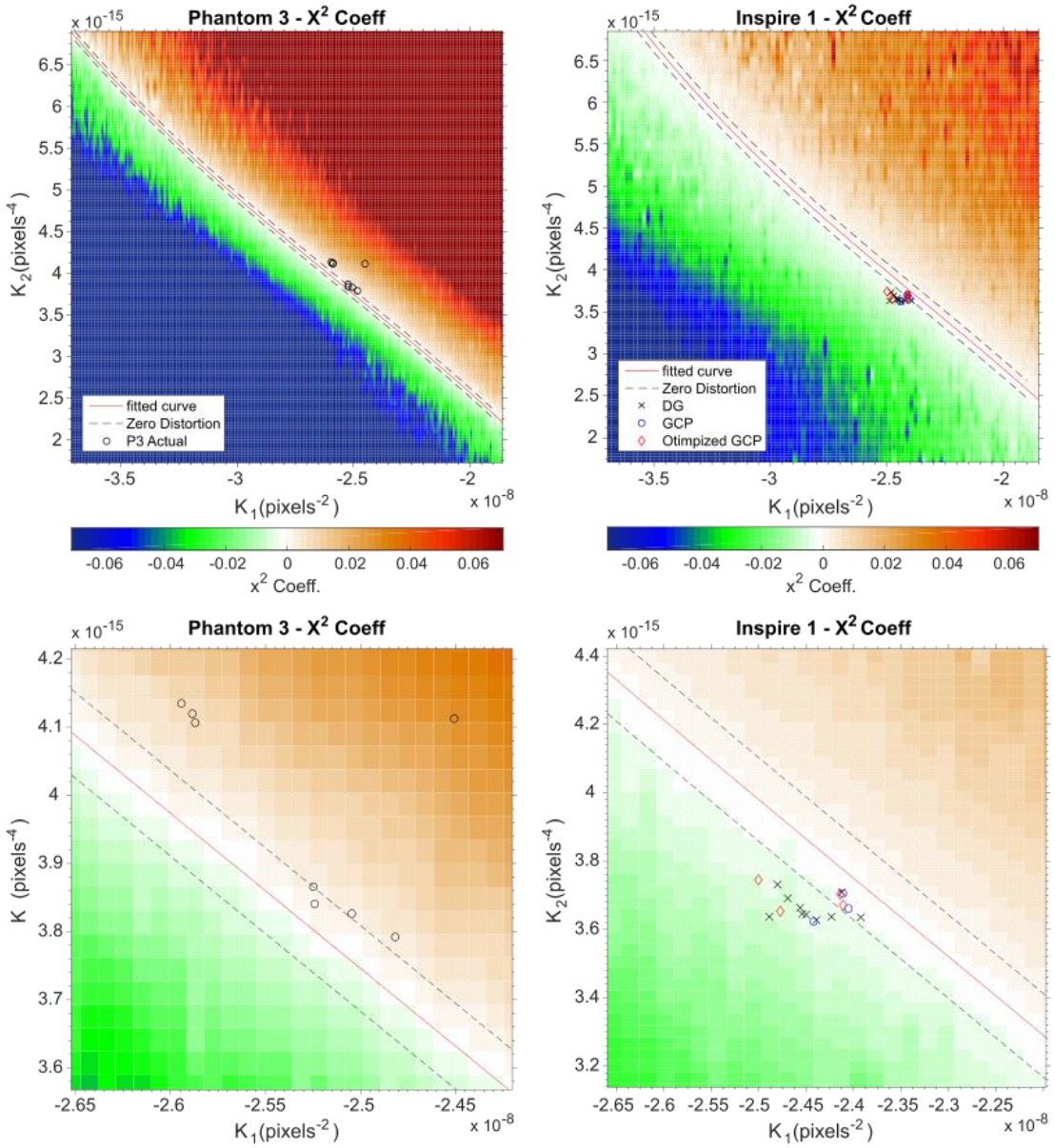

Figure 6. Perturbation outputs of surface doming as a function of K_1, K_2 for the Phantom 3 and the Inspire 1. The color ramps represent the magnitude of x^2 coefficients from the polynomial fits. The central diagonal bands with null x^2 coefficients are interpreted as families of K_1-K_2 solutions that sucessfully model lens distortion and eliminate parabolic doming. Points added to each surface represent calibrated (K_1,K_2) values for real data. In the case of the Phantom 3 surface, these are the outputs for all 11 direct georeferencing (DG) flight experiments. In the case of the Inspire 1, these represent other data not discussed in this paper and they use a DG, traditional GCP and software optimisation (a Photoscan function).

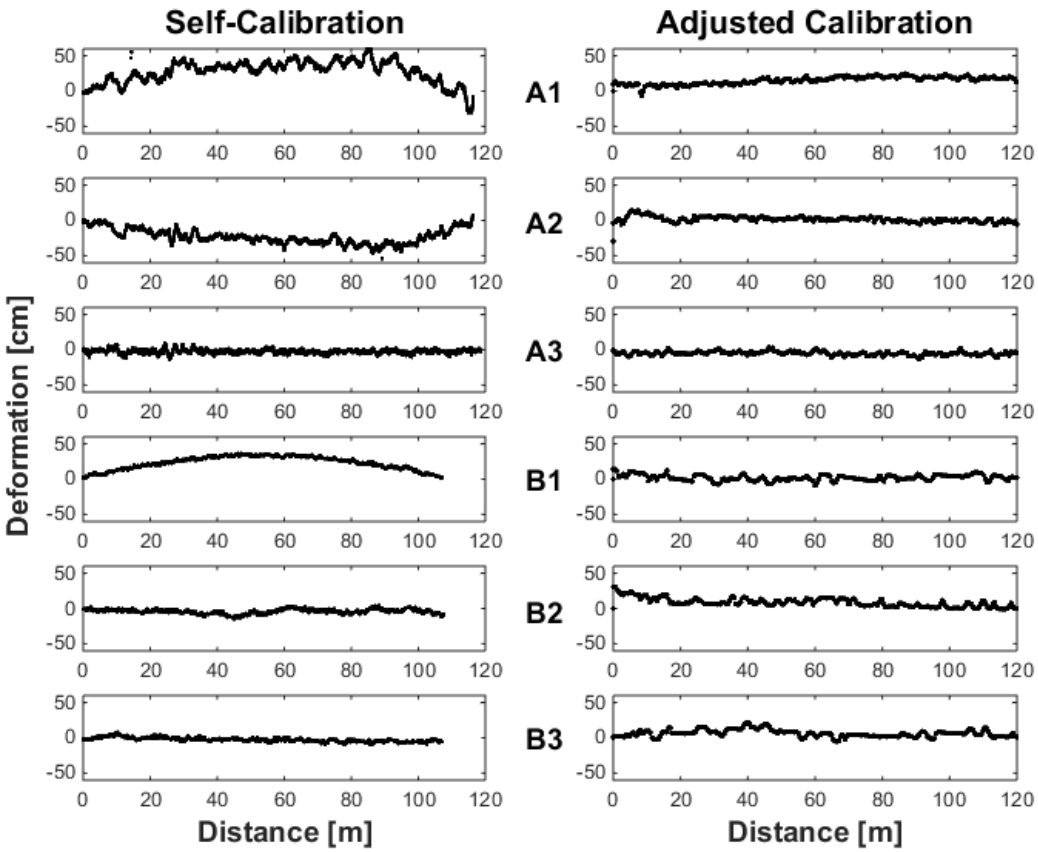

Figure 7. Linear profiles from α to β with self-calibrated and adjusted calibration values. Deformation amplitude is calculated by comparing sites A1-A3 to the optimal A4 and B1-B3 to the optimal B4. We note that whilst doming is eliminated, the adjustment results in increased surface noise.

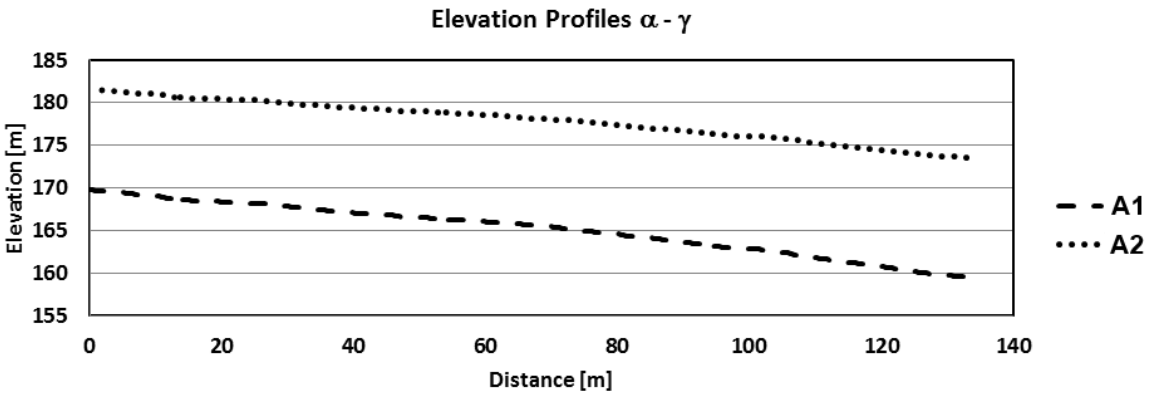

Figure 8. Effects of focal length calibration errors on datum along α–γ. Note that profile length in XY is not affected.

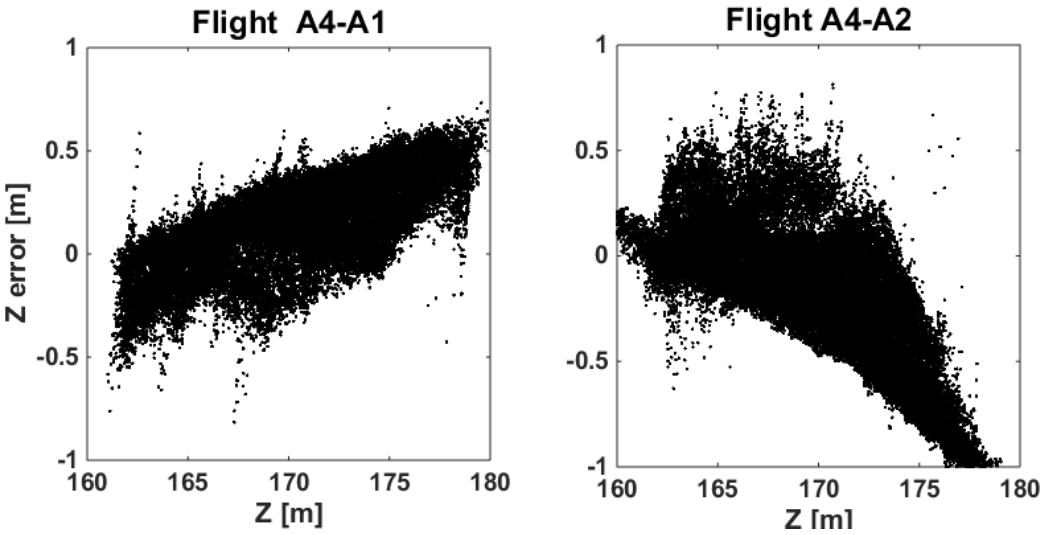

Figure 9. Altitude dependent errors. Here we show the correlation between absolute altitude and error for flights A1 and A2 which had the poorest calibration of focal length.

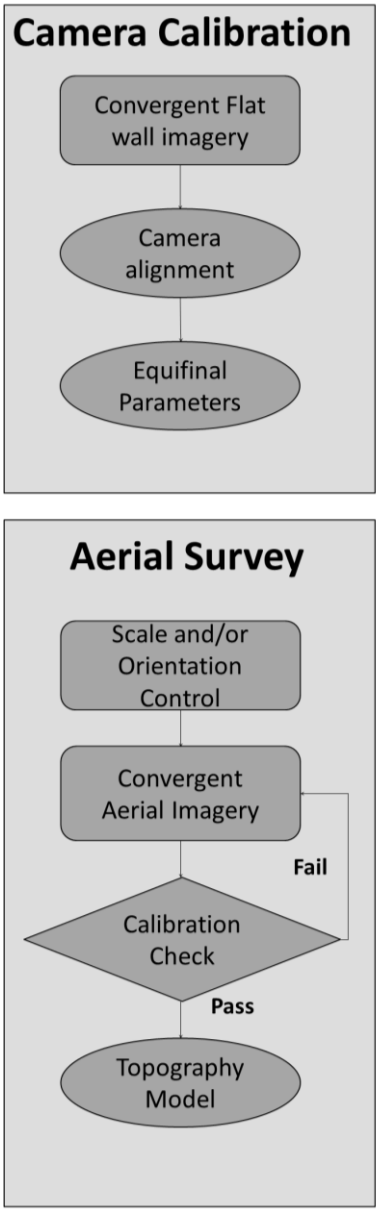

Figure 10. Summarised DG workflow. The two stages of the proposed workflow. The camera calibration stage aims to identify the focal length and the set of equifinal solutions along with their domain of applicability. This information can then be used in the calibration check, potentially carried out in the field, that allows for a reliable topographic model to be produced with a direct georeferencing.